IAES International Journal of Artificial Intelligence (IJ-AI)
Vol. 15, No. 2, April 2026, pp. 1451~1463
ISSN: 2252-8938, DOI: 10.11591/ijai.v15.i2.pp1451-1463

Exponential long short-term memory with Levy flight optimization for lung nodule classification

Kaliba Gowthami, Kamalakannan Jayaseelan
School of Computer Science Engineering and Information System, Vellore Institute of Technology, Vellore, India

Article Info

Article history:

Received Jul 18, 2025
Revised Jan 9, 2026
Accepted Jan 25, 2026

Keywords:

Archimedes optimization algorithm
Bayesian active contour
Dynamic Levy flight
Exponential linear unit
Long short-term memory
Lung nodule

ABSTRACT

Lung cancer, which commonly appears as lung nodules is a deadly type of cancer that develops in a lung. Early detection of lung cancer is critical and challenging task due to presence of overlapping structures, which make it challenging to differentiate the benign and malignant regions. This research proposes long short-term memory (LSTM) with exponential linear unit (ELU) method for the classification of different classes of lung nodules. The hyperparameters of the LSTM network are optimized using the developed dynamic Levy flight – Archimedes optimization algorithm (DLF-AOA), which effectively identifies the optimal parameters for classification. The ResNet-18 method is used for the extraction of high-level features to differentiate various classes of lung nodules. Furthermore, Bayesian active contour (BAC) is employed for the segmentation of images as containing cancerous and non-cancerous regions of lung nodules. The LSTM with ELU method achieves 98.56% accuracy, 97.54% sensitivity, 98.22% specificity, 96.93% precision, 96.33% F1-score, and 1.44 error rate in IQ-OTH/NCCD lung cancer dataset.

Corresponding Author:

Kaliba Gowthami
School of Computer Science Engineering and Information System, Vellore Institute of Technology
Vellore, India
Email: gowthami.k2022@vitstudent.ac.in

1. INTRODUCTION

Lung cancer is a deadliest type of cancer worldwide. However, early detection of lung cancer can significantly improve survival rate [1]. The malignant (cancerous) and benign (non-cancerous) pulmonary nodules are small growth of cells in the lungs [2]. The detection of malignant lung nodules in the initial phase is essential for effective prognosis [3]. In the initial phase, cancerous lung nodules can appear similar to non-cancerous nodules, but require differential diagnosis based on subtle morphological changes, positions and clinical biomarkers [4]–[6]. One of the most challenging aspects is to calculate the probability of malignancy in early-stage cancerous lung nodules [7]. Various diagnostics methods, including computed tomography (CT) scan analysis and positron emission tomography (PET) have been utilized by physicians for the initial diagnosis of malignant lung nodules [8]. Additionally, many invasive techniques such as surgeries or biopsies are utilized by healthcare practitioners for differentiating between malignant and benign lung nodules [9]. Given the sensitivity of fragile organs like the lungs, these invasive techniques carry high risks and increase patient anxiety. The most suitable technique for investigating lung diseases is through CT images [10].

Researchers have developed many segmentation techniques to assist radiologists in detecting lung cancerous tumors [11]. The lung cancer segmentation techniques are separated into two main categories: classical algorithms and deep learning (DL) algorithms [12]. Classical algorithms primarily focus on intensity-based techniques such as region growth, adaptive threshold, morphological technique, active-contour method and shape analysis [13]. However, these techniques are not effective in differentiating the tumor sizes and are not suitable for the segmentation of lung tumors [14]. Additionally, when tumors are integrated with various organs, the performance of tumor segmentation techniques is affected, resulting in a lower level of automation [15]. Hence, classical methods have been replaced with DL algorithms for countering numerous issues in image recognition [16]. The DL algorithms effectively extract significant features, without the need for human intervention [17], [18].

Tofighi *et al.* [19] introduced a MobileNetV2-stacked gated recurrent unit (SGRU), a novel transfer learning-enabled predictor to lung cancer classification. The introduced method was employed for the automatic extraction of features from lung CT images. However, introduced method did not remove noise from the images which minimized its classification performance. Ma *et al.* [20] suggested a convolutional neural network (CNN) framework and GoogLeNet with adaptive layers (GoogLeNet-AL) to lung cancer detection. The suggested method enhanced the overall capability of the model to capture the relevant features with intricate patterns. However, the suggested method failed to address the issue of vanishing gradients in the training phase, thereby minimizing classification performance. Kumaran *et al.* [21] integrated DL-based algorithm with pre-trained methods like ResNet-50, InceptionV3, and VGG-16 for enhanced lung cancer diagnostic accuracy. This model maximized the capability to discern subtle patterns in different lung features, but the model parameters were not sufficiently optimized for classification. Sabzalian *et al.* [22] implemented a bidirectional recurrent neural network (RNN) for accurate diagnosis of lung cancers. An enhanced form of the Ebola optimization search algorithm was employed in a setup to minimize execution costs by eliminating the requirement for exhaustive search techniques. However, the implemented method failed to segment the regions of lung nodules effectively, minimizing its capability to differentiate cancerous and non-cancerous regions. Raza *et al.* [23] presented a novel transfer learning-based predictor known as Lung-EffNet to classify lung cancers. The presented method developed on the structure of EfficientNet with further modifications that included the top layers for classification. However, the presented method did not extract high-level features necessary to identify the cancerous and non-cancerous regions.

On analysis of the existing algorithms, the following limitations have been noted: failure to remove noise from images, the inability to address the vanishing gradient issue during the training phase, lack of proper optimization of model parameters, ineffective segmentation of lung nodules, and insufficient extraction of high-level features. To mitigate these limitations, this article utilizes the Wiener filter and contrast limited adaptive histogram equalization (CLAHE) as pre-processing techniques to remove noise and enhance image contrast. Then, segmentation process is performed using Bayesian active contour (BAC) techniques, which effectively segment cancerous from non-cancerous regions. Then, the CNN-based pre-trained model is employed for the extraction of both low-level and high-level attributes to accurately identify and differentiate various regions within the image. Finally, classification is carried out using long short-term memory (LSTM) with the exponential linear unit (ELU) method, which effectively classifies lung nodule types. In addition, the hyperparameters of the LSTM are optimized using the dynamic Levy flight (DLF) with Archimedes optimization algorithm (AOA), which identifies the optimal parameters for the classification process. These DL-based algorithms enhance the accuracy of disease detection in medical field.

In this article, the DLF method introduces random large jumps based on Levy distribution, which enhances the algorithm's ability to escape suboptimal solutions during hyperparameter tuning. Unlike other optimization algorithms, such as whale optimization algorithm (WOA), genetic algorithm (GA), or particle swarm optimization (PSO), which rely on fixed step sizes, the DLF algorithm dynamically adjusts hyperparameters by balancing global exploration and fine-tuned local search. The AOA ensures effective exploitation, while DLF accelerates convergence by improving search diversity. Unlike existing lung nodule classification models which address segmentation, feature extraction or classification, this work introduced model which integrates BAC-based segmentation, deep residual feature extraction and sequence-aware LSTM classification optimized by DLF-AOA. The proposed DLF-AOA ensures adaptive exploration and exploitation in hyperparameter tuning. Moreover, combination of ELU in LSTM model efficiently overcomes vanishing gradient problems leads to stable training and enhanced discrimination among benign, malignant and normal nodules. The crucial contributions of this article are outlined as follows:

i) The BAC method is used for segmentation to distinguish the cancerous from non-cancerous regions in lung nodules.
ii) The LSTM network with ELU activation function is employed for classifying different types of lung nodules, mitigating the vanishing gradient issue and enhancing classification performance.
iii) The optimal parameters of the LSTM network for lung nodule classification are identified using the DLF–AOA, which helps improve classification accuracy.

This research paper is further organized as follows: section 2 details proposed technique. Section 3 provides the results and a discussion of the proposed technique. Finally, section 4 concludes the research.

2. METHOD

An efficient DL-based model is developed for classification of various classes of lung nodules. The IQ-OTH/NCCD lung cancer dataset with images pre-processed using a wiener filter for noise removal and CLAHE used for enhancing image quality is used in this research. Furthermore, BAC-based segmentation is performed to segment the images into pixels for the identification of cancerous and non-cancerous regions. ResNet-18 based feature extraction model is used to capture low-level and high-level features for differentiating classes. Finally, the LSTM with ELU method is developed to accurately classify different classes of lung nodules, besides the optimal parameters identified using DLF with AOA. Figure 1 illustrates the process of lung nodules classification.

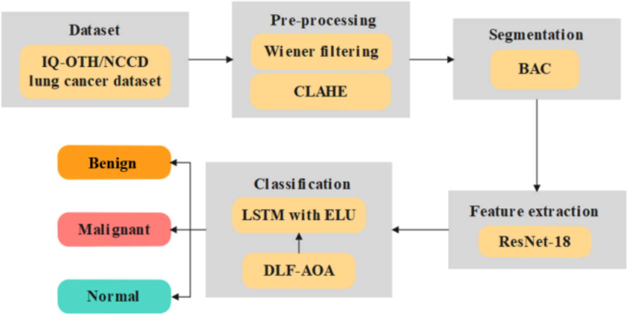

Figure 1. Process of lung nodule classification

2.1. Dataset

IQ-OTH/NCCD lung cancer dataset [24] utilized in this study classifies image data into three categories: benign, malignant, and normal. The images exhibit various differences in both dimensions and labels, which reflect layered complexity. The standard image size in a dataset is 512×512 pixels. The dataset includes 120 benign samples, each with a size of 512×512 pixels. For the malignant class, there are 561 samples: 501 are 512×512 pixels, 31 are 512×623 pixels, 28 are 512×801 pixels, and one is 404×511 pixels. The normal class contains 416 samples, with 415 being 512×512 pixels and one being 331×506 pixels. The distribution of a dataset is shown in Table 1 and Figure 2 illustrates sample images from the dataset.

Table 1. Dataset distribution

Type of classes	Number of samples
Benign	120
Malignant	561
Normal	416

Figure 2. Sample images in the dataset

2.2. Pre-processing

The dataset includes 1,000 CT images in .jpg format, classified into 4 categories: large cell carcinoma, squamous cell carcinoma, normal, and adenocarcinoma. The images in a dataset are pre-processed by Wiener filter and contrast enhancement techniques, which remove noise and enhance image contrast. A detailed explanation of these pre-processing methods is provided as:

i) Wiener filter: the Wiener filter computes an optimum tradeoff between inverse filtering and noise smoothing. This filter eliminates additional noise, inverts blurring, and reduces overall mean square error (MSE) during inverse filtering and noise smoothing. The mathematical formula for the filtering process is given in (1).

$$f(x,y) = \frac{H\times(f_1,f_2)S_{xx}(f_1,f_2)}{H(f_1,f_2)2S_{xx}(f_1,f_2)+S_{nn}(f_1,f_2)} \tag{1}$$

ii) Contrast enhancement: this phase enhances perception for further processing by sharpening image borders and maximizing accuracy with an emphasis on brightness variance between the foreground and background. Besides, CLAHE is utilized to limit contrast amplification for noise removal. In medical images, it enhances the local details while maintaining smoothness in areas without significant modifications. The pre-processed images are fed into the segmentation process to separate the diseased and non-diseased regions of the lung nodules. Figure 3 illustrates the pre-processed images.


Benign Malignant Normal

Figure 3. Pre-processed images

2.3. Segmentation

The BAC method is used in this phase, which incorporates a Bayesian framework that includes prior knowledge, making it robust for overlapping lung structures and varying tumor shapes. This is particularly beneficial when annotated data is limited, as it is resilient to noise, preserves edges, and performs well with small datasets. Consider N CT image frames, where a lung contour of a n^th image is represented by the state vector C_F^n. Each frame corresponds to a spatially sliced image from top to bottom. State vector C_F^n is then evolved using (2).

$$C_F^n = f_n(C_F^{n-1}, w^n) \tag{2}$$

Where f_n represents a transition function corresponding to the change of lung contour from $(\mathrm{n}-1)$th image. Noise term w^n represents zero-mean, independent white-noise, unaffected by both previous and present states. In Bayesian method, measurement vector is relevance to state vector C_F^n through observation equation. The measurement vector is represented as C_G^n. The observation equation is given in (3).

$$C_G^n = h_n(C_F^n, v^n) \tag{3}$$

Where h_n represents measurement function and v^n represents noise which is a zero-mean sequence, independent white noise, unrelated to both previous and current states, as well as system noise. Initial probability density function (PDF) is represented as $\rho(C_F^1|C_G^0) = \rho(C_F^1)$. The available data in nth frame is set to a measurement vector. The objective is to develop a PDF of state vector C_F^n, based on all available data, which is acquired recursively in two phases of update and prediction. Required PDF and previous PDF of the state vector C_F^n is attained using (4) and (5).

$$\rho(C_F^n|D^{n-1}) = \int \rho(C_F^n|D_F^{n-1})\rho(C_F^{n-1}|D^{n-1})dC_F^{n-1} \tag{4}$$

Since the $\rho(w^n|C_F^{n-1}) = \rho(w^n)$.

$$\rho(C_F^n|C_F^{n-1}) = \int \delta\big(C_F^n - f_n(C_F^{n-1}, w^n)\big)\rho(w^n)dw^n \tag{5}$$

Where $\delta(.)$ represents a dirac delta function. In nth frame, C_G^n represents the measurement vector presented and utilized for updating the previous PDF for posterior PDF in accordance with the Bayes' rule, as mathematically formulated in (6). The mathematical formula for denominator normalizing is given as in (7). The mathematical formula for PDF condition is represented through measurement function, as given in (8).

$$\rho(C_F^n|D^n) = \frac{\rho(C_G^n|C_F^n)\rho(C_F^n|D^{n-1})}{\rho(C_G^n|D^{n-1})} \quad (6)$$

$$\rho(C_G^n|D^{n-1}) = \int \rho(C_G^n|C_F^n)\rho(C_F^n|D^n)dC_F^n \quad (7)$$

$$\rho(C_G^n|C_F^n) = \int \delta(C_G^n - h_n(C_F^n, v^n))\rho(v^n)dv^n \quad (8)$$

Where C_G^n represents the measurement vector utilized to modify the predicted previous PDF for obtaining the subsequently required PDF of a C_F^n state vector. Next, an updated PDF is utilized for a previous PDF in $n+1$ th frame. The recurrent relations of equations establish a general solution for Bayesian recursive evaluation issues.

2.4. Feature extraction

The segmented images are input for feature extraction, where meaningful and deep features of the lung nodules are extracted using the ResNet-18 method. ResNet-18 leverages residual connections, which help mitigate the vanishing gradient issue and enhance deep feature learning. ResNet is a residual network with an 18-layer CNN pre-trained model. In this study, ResNet-18 utilizes 3×3 filters with a stride and padding of 1, an average pooling layer with a 1×1 filter, 1 fully connected layer, and a final SoftMax layer. The ResNet-18 includes four major phases where every phase contains a multi-residual block. These blocks utilize skip connections which allow data for bypassing some layers, thereby assisting the network in learning deep features by mitigating vanishing gradients, proving advantageous in identifying the relevant structures. After every residual block, the pooling layer minimizes the spatial dimensions of features and concentrates on the significant data, making the network more robust to spatial differences in the input. After final convolutional block, global average pooling is employed to efficaciously obtain feature vectors which describes the entire image in a condensed format.

2.5. Classification using long short-term memory with exponential linear unit

RNNs are kind of deep neural network (DNN) which establish connections between neurons within the same layer, making them suitable for time-series tasks. LSTM is a variant of RNN that addresses data redundancy by incorporating a "gate" architecture at strategic positions. This allows the network to selectively retain or discard data as it flows through each neuron. LSTMs are effective in overcoming issues such as vanishing gradients and exploding gradients, which commonly affect traditional RNNs [25]. Moreover, they excel in handling long-term dependencies in the data. The W_i and b_i is weight and bias of a input gate, the W_o and b_o is weight and bias of a output gate, W_c and b_c is weight and bias of a cell states, W_f and b_f is weight and bias of forget gate. The h_{t-1} is output of previous time step, while x_t is input of current time step. The developed new vector is denoted as $[h_{t-1}, x_t]$. The process of matrix multiplication of $[h_{t-1}, x_t]$ vector with W_c and b_c through the tanh activation function is used to obtain the input, as described in (9). The weights and parameter terms of each gate are processed through the sigmoid function to produce the forget, input, and output gates. The mathematical formulas for these gates are provided in (10) to (12).

$$C_t' = tanh(W_c \cdot [h_{t-1}, x_t] + b_c) \quad (9)$$

$$f_t = \sigma\left(W_f \cdot [h_{t-1}, x_t] + b_f\right) \quad (10)$$

$$i_t = \sigma(W_i \cdot [h_{t-1}, x_t] + b_i) \quad (11)$$

$$o_t = elu(W_o \cdot [h_{t-1}, x_t] + b_o) \quad (12)$$

By multiplying f_t with the previous cell state C_{t-1}, the data to be forgotten and remembered is determined, thereby controlling C_{t-1}. By multiplying i_t with the current input cell state C_t', the data C_t' required to be stored and used is determined. Finally, the state value of the hidden layer at time t is obtained by adding two products, as shown in (13). Finally, result at time t is determined by unit state, output gate, and tanh activation function, as described in (14).

$$C_t = f_t \times C_{t-1} + i_t \times C_t' \quad (13)$$

$$h_t = o_t \times tanh(C_t) \quad (14)$$

2.5.1. Exponential linear unit

The ELU integrates two activation functions, rectified linear unit (ReLU) and sigmoid. The activation function is used to weigh the integration of sources or results applied in the subsequent phase. The output of this function fluctuates between 0 and 1 when the perceptron is a mathematical function. ELU differs from ReLU by allowing negative values. It offers a lower execution cost compared to batch normalization and results in higher average unit activation, which is closer to 0. The hyperparameter α controls the saturation value of the ELU for negative inputs. The mathematical formulas for ELU activation function are given in (15) and (16).

$$f(x) = \begin{cases} x, & x > 0 \\ \alpha(exp(x) - 1), & x \leq 0 \end{cases} \tag{15}$$

$$f'(x) = \begin{cases} 1, & x > 0 \\ f(x) + \alpha, & x \leq 0 \end{cases} \tag{16}$$

Compared to other activation functions, the ELU enhances learning characteristics at all times and achieves an average activation closer to 0, which accelerates learning. The ELU activation reduces the difference in forward propagation and the data transferred to the next layer, even when the input parameters are limited. In this paper, the ELU is used instead of the sigmoid, offering both robustness and reduced complexity. This simplifies the process and addresses the issue of vanishing gradients.

2.5.2. Hyperparameter tuning using dynamic Levy flight with Archimedes optimization algorithm

In this article, the DLF introduces random large jumps based on the Levy distribution, enhancing the capability to escape poor solutions during hyperparameter tuning. Unlike other optimization algorithms such as WOA, GA, or PSO, which rely on fixed step sizes, DLF-AOA dynamically adjusts hyperparameters by balancing global exploration and fine-tuned local search. The AOA ensures effective exploitation, while DLF accelerates convergence by improving search diversity. AOA is a population-based algorithm, where individuals in the population are focused on specific objectives. Similar to other population-based algorithms, AOA drives the process with a main population of individuals that are subject to random accelerations, densities, and volumes. The AOA begins by evaluating the fitness of the preliminary population and continues iterating until termination condition is met. In every iteration, volume and density of individuals are updated. The individual's acceleration is revised based on their interaction with neighboring individuals, and the updated density, volume, and acceleration determine new position of the individual. Mathematical formula for initialization is provided in (17).

$$x_i = ll_i + rand \times (ul_i \times ll_i),\ i = 1,2,\ldots,N \tag{17}$$

Where N is number of individuals in population, x_i is the ith individual, ll_i represents the lower limit, ul_i represents the upper limit of the search area, and $rand$ represents the dimension vector arbitrarily given in the range [0, 1]. The mathematical formula for reset density for every ith individual is given in (18). Finally, the initial acceleration of the ith parameter and its mathematical formula are given in (19). In this phase, the initial population is evaluated and relevant individuals that have optimal fitness values are selected. Then, x_{best}, d_{best}, v_{best}, and a_{best} are employed, where x_{best} represents the optimal individual, d_{best}, v_{best}, and a_{best} represent density, volume, and acceleration relevance with a fitness value.

$$d_i = rand, v_i = rand \tag{18}$$

$$ac_i = ll_i + rand \times (ul_i \times ll_i) \tag{19}$$

i) Renew volumes and densities: density and volume of the individual i in repetition $t + 1$ and its mathematical formula is given as (20) and (21). Where d_{best} and v_{best} represent density and volume relevance. With an optimal individual, distributed uniformly as the random number is represented as $rand$.

$$d_i^{t+1} = d_i^t + rand(d_{best} - d_i^t) \tag{20}$$

$$v_i^{t+1} = v_i^t + rand(v_{best} - v_i^t) \tag{21}$$

ii) Density factor and transfer operator: initially, individuals collide, and over time, they attempt to converge toward a symmetric state. In AOA, this process is facilitated by the transfer operator, that shifts the focus from exploration to exploitation. The mathematical formula for the transfer operator is given in (22). In the (22), t is number of iterations and t_{max} is maximum iterations. The density declining factor (ddf) helps the AOA in global and local searches, and its mathematical formula is given in (23). In the (23), ddf^{t+1} represents the declining time which gives the model the ability to converge in past recognized regions. This represents the suitable handling of the variation to strike a balance among exploitation and exploration phases in AOA algorithm.

$$TO = exp\left(\frac{t-t_{max}}{t_{max}}\right) \tag{22}$$

$$ddf^{t+1} = exp\left(\frac{t_{max}-t}{t_{max}}\right) - \left(\frac{t}{t_{max}}\right) \tag{23}$$

iii) Exploration phase (collision among individuals): when $TO \leq 0.5$, there is a collision among individuals, and so a random material is selected and acceleration of the parameter for $t+1$ repetition is revised, as shown in (24). In the (24), d_i represents density, v_i represents the volume, and ac_i represents acceleration of ith individual. This is essential for representation as $TO \leq 0.5$, which guarantees exploration at time of 1/3 iteration.

$$ac_i^{t+1} = \frac{d_{mr}+v_{mr}+ac_{mr}}{d_i^{t+1}+v_i^{t+1}} \tag{24}$$

iv) Exploitation stage (null collision among individuals): in condition $TO > 0.5$, there is null collision between individuals, revising the acceleration of individuals for iteration $(t+1)$, as mathematically formulated in (25). By using (26), acceleration is required to be normalized for executing the variation proportion. In the (26), $u = 0.9$ and $l = 0.1$ represent the normalization range. The ac_{i-norm}^{t+1} represents the ratio of phases in which each agent varies. In the condition where i is an individual that is afield from the global optimum, the value of acceleration is high, meaning that individual remains in exploitation or exploration stage and path of exploration transitions from a stage of exploration to exploitation. Under general conditions, an acceleration component initiates with higher value which declines with time. This helps the search agents in navigating toward the global optimal outcomes and away from local solutions. The key observation is that there are a few search agents that require extra time for the exploration phase compared to general circumstances. Hence, the symbiotic organisms search (SOS) provides stability in both exploitation and exploration.

$$ac_i^{t+1} = \frac{d_{best}+v_{bext}+ac_{best}}{d_i^{t+1}+v_i^{t+1}} \tag{25}$$

$$ac_{i-norm}^{t+1} = u \times \frac{ac_i^{t+1}-min\,(ac)}{max(ac)+min\,(ac)} \tag{26}$$

v) Update position: when $TO \leq 0.5$, the position of individual i for a next iteration $t+1$ is given as in (27). In the (27), Con_1 represents a constant set to 2. Alternatively, when $TO > 0.5$, individuals revise their positions, as mathematically formulated in (28). In the (28), Con_2 represents a constant set to 6. T, proportional to TO, is defined using $T = Con_3 \times TO$. Where, Con_3 represents a constant set to 2. As T increases, it considers the time limit and the ratio from the optimal position. It starts with small ratios, resulting in a high variance concern in the step-size of random walk between the optimal and current locations. As a search progresses, this ratio increases, reducing the variance between the optimal position and the present state, thereby achieving an appropriate equilibrium between exploitation and exploration. The K flag indicates various directions of motion, and its mathematical formula is given in (29). In the (29), $q = 2 \times rand - Con_4$ and Con_4 represent a constant equal to 0.5. Each parameter is evaluated using the fitness function and record the optimal output obtained so far. The values of $x_{best}, d_{best}, v_{best}$ and ac_{best} are allocated.

$$x_i^{t+1} = x_i^t + Con_1 \times rand \times ac_{i-norm}^{t+1} \times ddf \times (x_{rand} - x_i^t) \tag{27}$$

$$x_i^{t+1} = x_{best}^{t+1} + K + Con_2 \times rand \times ac_{i-norm}^{t+1} \times ddf \times (T \times x_{best} - x_i^t) \tag{28}$$

$$k = \{+1\ if\ q \leq 0.5\ and -1\ if\ q > 0.5\} \tag{29}$$

vi) DLF with AOA: in this section, dynamic features are employed for the solutions in AOA. Metaheuristic algorithms generally consist of two primary phases: exploration and exploitation, which maintain an optimal balance between them. In this paper, the dynamic version is utilized to emphasize both exploitation and exploration, where each solution dynamically updates its position based on the best solution attained during the optimization process. The dynamic candidate solution (DCS) function is incorporated with the Levy flight function, replacing (25) and (26). The updated mathematical formulas are provided in (30) and (31). The DCS function is implemented to account for the effect of decreasing the percentage in the candidate solution during each iteration. Its values are given in (32) and (33).

$$ac_i^{t+1} = \frac{d_{best}+v_{best}+ac_{best}}{d_i^{t+1}+v_i^{t+1}} + LF \times DCS \tag{30}$$

$$ac_{i-norm}^{t+1} = u \times \frac{ac_i^{t+1}-min\,(ac)}{max(ac)+min\,(ac)} + LF \times DCS \tag{31}$$

$$DCS(0) = 1 - \sqrt{\frac{Iter}{Iter_{Max}}} \tag{32}$$

$$DCS(t+1) = DCS(t) \times 0.99 \tag{33}$$

3. RESULTS AND DISCUSSION

The performance of DLF with AOA and ELU based LSTM method is simulated in MATLAB 2020b. The system is configured with i5 processor, Windows 10 (64 bit) and 8 GB RAM. Performance of a developed model is evaluated in terms of the performance metrics of accuracy, sensitivity, specificity, precision, F1-score, and error rate.

In Table 2, performance of a developed DLF with AOA based hyperparameter tuning process is evaluated based on various performance metrics. The different optimization algorithms utilized to evaluate the performance of DLF with AOA are, PSO, ant colony optimization (ACO), grey wolf optimization algorithm (GOA), and pelican optimization algorithm (POA). The DLF with AOA based hyperparameter tuning process attains 98.56% accuracy, 97.54% sensitivity, 98.22% specificity, 96.93% precision, 96.33% F1-score, and 1.44 error rate. The DLF is incorporated into traditional AOA to enhance exploration by introducing random perturbations based on the Levy flight distribution, which improves global search capabilities. Rather than directly updating based on acceleration, DLF dynamically adjusts the step size, enabling fine-tuning of hyperparameters. In Table 3, performance of an ELU activation function is evaluated with various performance metrics. The different activation functions utilized to evaluate the performance of ELU include ReLU, Leaky ReLU, Tan, and Sin. The ELU activation function achieves 98.56% accuracy, 97.54% sensitivity, 98.22% specificity, 96.93% precision, 96.33% F1-score, and 1.44 of error rate.

Table 2. Performance of developed DLF with AOA method

Methods	Accuracy (%)	Sensitivity (%)	Specificity (%)	Precision (%)	F1-score (%)	Error rate
IQ-OTH/NCCD lung cancer dataset						
PSO	93.58	94.22	95.11	93.34	92.48	6.41
ACO	90.11	93.47	90.11	91.30	89.22	9.88
GOA	95.22	92.77	89.77	92.38	92.00	4.77
POA	96.44	94.27	95.02	94.06	93.89	3.55
DLF-AOA	98.56	97.54	98.22	96.93	96.33	1.44
Chest CT-scan image dataset						
PSO	94.58	95.22	96.11	94.34	93.48	7.41
ACO	91.11	94.47	91.11	91.40	90.22	9.98
GOA	96.22	93.77	90.77	95.38	95.00	5.77
POA	98.74	98.56	97.93	99.74	98.16	1.12
DLF-AOA	99.46	99.14	98.22	99.23	98.83	1.74

In Table 4, the performance of LSTM with ELU method is validated by various performance metrics. The different classifiers used to evaluate the performance of LSTM with ELU include sparse auto-encoder (Sparse AE), traditional LSTM, neural network (NN), and DNN. The LSTM with ELU method achieved 98.56% accuracy, 97.54% sensitivity, 98.22% specificity, 96.93% precision, 96.33% F1-score, and an error rate of 1.44. In Table 5, performance of a LSTM with ELU method is validated using various performance metrics with different k-fold values, ranging from k =3 to k =7. The LSTM with the ELU method achieves 98.56% accuracy, 97.54% sensitivity, 98.22% specificity, 96.93% precision, 96.33% F1-score, and an error rate of 1.44 at a k value of 5.

Table 3. Performance of ELU activation function

Methods	Accuracy (%)	Sensitivity (%)	Specificity (%)	Precision (%)	F1-score (%)	Error rate
IQ-OTH/NCCD lung cancer dataset						
ReLU	91.48	89.47	90.55	88.57	87.69	8.51
Leaky ReLU	92.58	82.74	88.47	83.91	85.12	7.41
Tan	88.12	85.78	82.69	80.30	75.48	11.87
Sin	80.23	81.45	82.77	80.97	80.48	19.76
ELU	98.56	97.54	98.22	96.93	96.33	1.44
Chest CT-scan image dataset						
ReLU	92.54	90.24	91.57	91.57	91.69	8.51
Leaky ReLU	93.58	83.74	89.47	93.31	93.12	7.41
Tan	89.12	85.78	82.69	88.30	76.48	11.87
Sin	81.23	82.45	83.77	80.97	80.48	19.76
ELU	99.46	99.14	98.22	99.23	98.83	1.74

Table 4. Performance of LSTM with ELU method

Methods	Accuracy (%)	Sensitivity (%)	Specificity (%)	Precision (%)	F1-score (%)	Error rate
IQ-OTH/NCCD lung cancer dataset						
Sparse AE	62.58	59.57	63.58	65.83	73.57	37.41
LSTM	96.58	89.41	93.66	89.73	90.05	3.41
NN	75.64	72.48	77.15	71.72	70.99	24.35
DNN	85.47	80.56	82.48	77.93	75.48	14.52
LSTM with ELU	98.56	97.54	98.22	96.93	96.33	1.44
Chest CT-Scan image dataset						
Sparse AE	73.58	60.57	63.75	73.24	73.57	38.41
LSTM	97.58	90.41	92.66	96.73	96.05	3.56
NN	75.64	72.24	75.56	75.72	75.99	34.14
DNN	86.47	81.56	82.48	85.93	85.48	12.14
LSTM with ELU	99.46	99.14	98.22	99.23	98.83	1.74

Table 5. Performance of LSTM with ELU method for K-fold values

K-values	Accuracy (%)	Sensitivity (%)	Specificity (%)	Precision (%)	F1-score (%)	Error rate
IQ-OTH/NCCD lung cancer dataset						
K=3	95.68	94.87	95.87	92.62	90.48	4.31
K=4	96.98	95.78	96.87	94.09	92.45	3.01
K=5	98.56	97.54	98.22	96.93	96.33	1.44
K=6	97.56	93.48	94.58	92.50	91.54	2.43
K=7	96.48	90.48	92.84	90.13	89.77	3.51
Chest CT-scan image dataset						
K=3	94.43	93.87	94.87	93.42	93.48	4.31
K=4	95.92	95.24	96.52	94.53	94.31	3.01
K=5	99.46	99.14	98.22	99.23	98.83	1.74
K=6	97.56	93.48	94.58	96.50	96.42	2.43
K=7	96.43	91.32	92.36	95.13	94.77	3.51

Figure 4 represents a confusion matrix for IQ-OTH/NCCD lung cancer dataset. Figure 5 represents a confusion matrix for the chest CT-scan image dataset. Figure 6 represents a receiver operating characteristic (ROC) curve for IQ-OTH/NCCD lung cancer dataset, while Figure 7 represents a ROC curve for the chest CT-scan image dataset. Table 6 shows the evaluation of computation time and memory usage for the proposed algorithm. Table 7 represents the cross-dataset generalization with training on IQ-OTH/NCCD lung cancer dataset and testing on chest CT-scan image dataset. Table 8 represents the cross-dataset generalization with training on chest CT-scan image dataset and testing on IQ-OTH/NCCD lung cancer dataset. Tables 7 and 8 represents the reliability of proposed model when analyzing unseen data from different clinical origins. Table 7 represents that LSTM with ELU model obtains high accuracy of 80.43% when trained on IQ-OTH/NCCD lung cancer dataset and tested on chest CT data. Table 8 shows high accuracy of 81.73%, as vice-versa of Table 7, shows model's capability to capture pathological markers than particular dataset features.

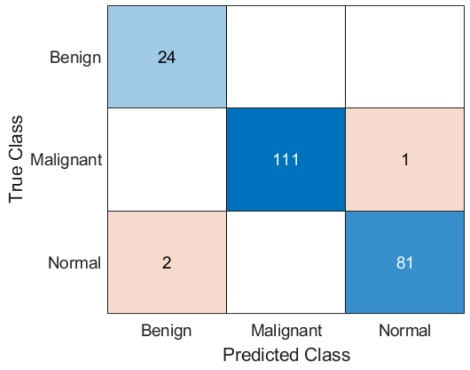

Figure 4. Confusion matrix for IQ-OTH/NCCD lung cancer dataset

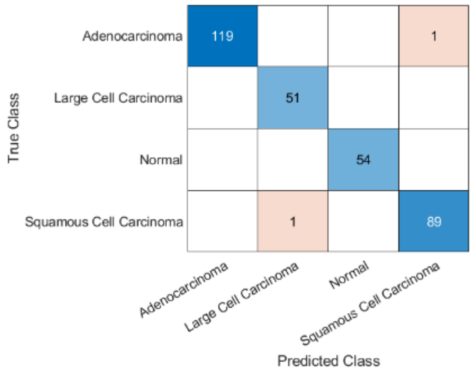

Figure 5. Confusion matrix for chest CT-scan image dataset

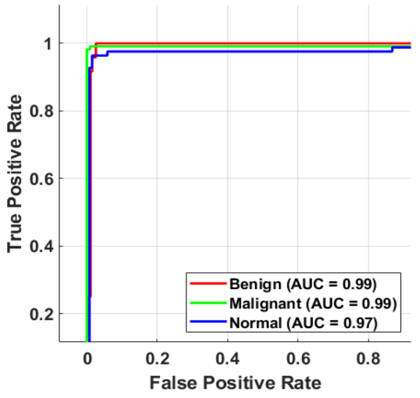

Figure 6. ROC curve for IQ-OTH/NCCD lung cancer dataset

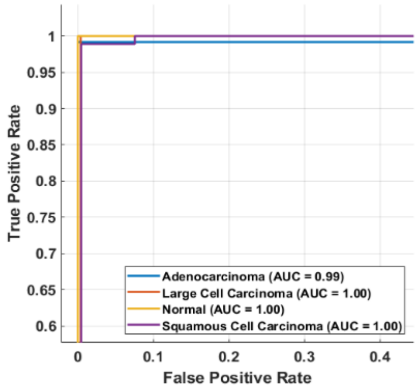

Figure 7. ROC curve for chest CT-scan image dataset

Table 6. Evaluation of computation time and memory usage

Methods	Dataset	Computation time (min)	Memory usage (MB)
Sparse AE	IQ-OTH/NCCD	29	240
LSTM		30	225
NN		25	207
DNN		27	183
LSTM with ELU		30	245
Sparse AE	Chest CT-scan	28	245
LSTM		35	230
NN		30	213
DNN		32	197
LSTM with ELU		35	250

Table 7. Cross dataset generalization with training on IQ-OTH/NCCD and testing on chest CT-scan

Methods	Accuracy (%)	Sensitivity (%)	Specificity (%)	Precision (%)	F1-score (%)
Sparse AE	77.41	77.27	76.84	76.47	76.22
LSTM	77.63	77.48	77.09	76.82	76.62
NN	78.16	77.65	77.34	77.02	76.83
DNN	78.64	78.25	78.02	77.62	77.48
LSTM with ELU	80.43	79.41	79.23	79.03	78.82

Table 8. Cross dataset generalization with training on chest CT-scan and testing on IQ-OTH/NCCD

Methods	Accuracy (%)	Sensitivity (%)	Specificity (%)	Precision (%)	F1-score (%)
Sparse AE	77.82	77.43	77.04	76.58	76.32
LSTM	78.09	77.86	77.62	77.29	77.02
NN	78.68	78.36	78.02	77.85	77.59
DNN	79.48	79.18	78.85	78.62	78.29
LSTM with ELU	81.73	80.65	80.28	79.84	79.52

3.1. Comparative analysis

The performance of developed DLF with AOA and ELU based LSTM is compared to existing techniques like MobileNetV2-SGRU [19], GoogleNet-AL [20], integrated DL algorithms [21], and differential evolution optimized symbiotic - bidirectional recurrent neural network (DEOS-BRNN) [22] on IQ-OTH/NCCD lung cancer dataset and chest CT-scan image dataset. The developed DLF with AOA and ELU based LSTM attained the highest accuracy of 98.56 % on IQ-OTH/NCCD lung cancer dataset. Table 9 represents a comparative analysis of developed DLF with AOA and ELU based LSTM models. The DCS and Levy flight functions are incorporated into the traditional AOA, which maximizes the convergence rate and searchability of AOA for the feature selection process. This process eliminates the irrelevant or inappropriate features from the whole feature subset and helps to maximize the classification process. In the classification process, the ELU activation function is used during the training process of the LSTM network, which mitigates the vanishing gradients issue and stabilizes the network during training. The LSTM with ELU method attained 98.56% accuracy on IQ-OTH/NCCD lung cancer dataset and 99.46% accuracy on chest CT-scan image dataset.

Table 9. Comparative analysis of developed technique

Methods	Dataset	Accuracy (%)	Precision (%)	Recall (%)	F1-score (%)	Specificity (%)
MobileNetV2-SGRU [19]	IQ-OTH/NCCD lung cancer dataset	96.83	96.78	96.83	96.78	NA
GoogleNet-AL [20]		97.32	99.45	98.2	98.82	97.63
Integrated DL algorithms [21]		98.18	NA	NA	NA	NA
DEOS-BRNN [22]		97.06	98.52	96.15	97.31	96.48
Proposed DLF with AOA and ELU based LSTM		98.56	96.93	97.54	96.33	98.22
GoogleNet-AL [20]	Chest CT-scan image dataset	98.74	99.74	98.56	98.96	97.93
Proposed DLF with AOA and ELU based LSTM		99.46	99.23	99.14	98.83	98.22

3.2. Discussion

Comparing with baseline optimization algorithms like PSO, ACO, GOA, and POA, the proposed DLF-AOA consistently obtains superior performance across both datasets in terms of accuracy and error rate. These improvements determined effectiveness of dynamic exploration and exploitation balancing in hyperparameter tuning. Moreover, when comparing with traditional classifiers and activation functions, ELU-based LSTM shows enhanced stability and discrimination ability, overcoming vanishing gradient issues. The consistent performance enhancements obtained across two datasets shows robustness and generalization capability of proposed model than dataset-specific optimization. By analyzing the outcomes, it is noted that the proposed DLF-AOA based LSTM with ELU method offers a higher classification performance in lung nodule detection. The outcomes represent that the developed method effectively captures high-level features and patterns in the dataset to effectively differentiate various lung cancer classes. In this study, the Wiener filter and CLAHE are utilized as pre-processing techniques to remove noise from images and enhance image contrast. Then, segmentation is performed using BAC techniques to segment cancerous and normal regions in the image to effectively differentiate the cancerous and non-cancerous regions. The CNN-based pre-trained model is used in the feature extraction phase to capture both low-level and high-level features, enabling the effective identification and differentiation of various regions in image patterns. Finally, classification is performed by using LSTM with the ELU method, which effectively classifies the classes of lung nodules. Furthermore, the hyperparameters of LSTM are optimized using the DLF with AOA, which identifies the optimal parameters for classification. The performance of the developed method is compared to existing algorithms MobileNetV2-SGRU [19], GoogleNet-AL [20], integrated DL algorithms [21], and DEOS-BRNN [22] on the IQ-OTH/NCCD lung cancer and chest CT-scan image datasets. When compared to existing algorithms, the developed method exhibits an effective performance due to its capability to capture and learn both low-level and high-level features, mitigating the vanishing gradient issue during training for lung nodule classification.

4. CONCLUSION

The early detection of lung cancer is essential yet challenging task due to the presence of overlapping structures, which makes it difficult to differentiate the benign and malignant cancerous regions. In this study, efficient DL-based algorithm with hyperparameter tuning is developed for lung nodule classification. The IQ-OTH/NCCD lung cancer dataset is used for collecting images pre-processed with Wiener filtering which eliminates noise from images, while CLAHE is used to enhance image quality. Then, the pre-processed images are segmented using the BAC method which segments images into multiple pixels to differentiate the classes. The low-level and high-level features are extracted using ResNet-18 model which effectively differentiates different classes of lung nodules and helps improve feature representation. Then, features are classified by LSTM with ELU, where ELU activation function mitigates the vanishing gradients issue and enhances classification performance. Further, the optimal parameters of the LSTM network are tuned using the developed DLF-AOA, which searches the optimal hyperparameters and helps enhance the classification performance. The LSTM with ELU method achieves 98.56% accuracy, 97.54% sensitivity, 98.22% specificity, 96.93% precision, 96.33% F1-score, and a 1.44 error rate on IQ-OTH/NCCD lung cancer dataset. Additionally, the LSTM with ELU method achieves 99.46% accuracy, 99.14% sensitivity, 98.22% specificity, 99.23% precision, 98.83% F1-score, and a 1.44 error rate on the chest CT-scan image dataset. As future work, different optimization algorithms will be explored to further enhance the classification performance of lung nodules.

FUNDING INFORMATION

Authors state no funding involved.

AUTHOR CONTRIBUTIONS STATEMENT

This journal uses the Contributor Roles Taxonomy (CRediT) to recognize individual author contributions, reduce authorship disputes, and facilitate collaboration.

Name of Author	C	M	So	Va	Fo	I	R	D	O	E	Vi	Su	P	Fu
Kaliba Gowthami	✓	✓	✓	✓	✓	✓		✓	✓					✓
Kamalakannan Jayaseelan		✓				✓	✓	✓		✓	✓	✓	✓	

C : **C**onceptualization
M : **M**ethodology
So : **So**ftware
Va : **Va**lidation
Fo : **Fo**rmal analysis

I : **I**nvestigation
R : **R**esources
D : **D**ata Curation
O : Writing - **O**riginal Draft
E : Writing - Review & **E**diting

Vi : **Vi**sualization
Su : **Su**pervision
P : **P**roject administration
Fu : **Fu**nding acquisition

CONFLICT OF INTEREST STATEMENT

The authors declare no conflict of interest.

DATA AVAILABILITY

The data that support the findings of this study are openly available in IQ-OTH/NCCD lung cancer dataset at https://www.kaggle.com/datasets/hamdallak/the-iqothnccd-lung-cancer-dataset, reference [24].

REFERENCES

[1] M. M. Musthafa, I. Manimozhi, T. R. Mahesh, and S. Guluwadi, “Optimizing double-layered convolutional neural networks for efficient lung cancer classification through hyperparameter optimization and advanced image pre-processing techniques,” *BMC Medical Informatics and Decision Making*, vol. 24, no. 1, 2024, doi: 10.1186/s12911-024-02553-9.

[2] Z. Guo, J. Yang, L. Zhao, J. Yuan, and H. Yu, “3D SAACNet with GBM for the classification of benign and malignant lung nodules,” *Computers in Biology and Medicine*, vol. 153, 2023, doi: 10.1016/j.compbiomed.2022.106532.

[3] R. Wu, C. Liang, Y. Li, X. Shi, J. Zhang, and H. Huang, “Self-supervised transfer learning framework driven by visual attention for benign–malignant lung nodule classification on chest CT,” *Expert Systems with Applications*, vol. 215, 2023, doi: 10.1016/j.eswa.2022.119339.

[4] P. Sengodan, K. Srinivasan, R. Pichamuthu, and S. Matheswaran, “Early detection and classification of malignant lung nodules from CT images: an optimal ensemble learning,” *Expert Systems with Applications*, vol. 229, 2023, doi: 10.1016/j.eswa.2023.120361.

[5] A. Halder and D. Dey, “Atrous convolution aided integrated framework for lung nodule segmentation and classification,” *Biomedical Signal Processing and Control*, vol. 82, 2023, doi: 10.1016/j.bspc.2022.104527.

[6] T. S. Prakash, A. S. Kumar, C. R. B. Durai, and S. Ashok, “Enhanced Elman spike neural network optimized with flamingo search optimization algorithm espoused lung cancer classification from CT images,” *Biomedical Signal Processing and Control*, vol. 84, 2023, doi: 10.1016/j.bspc.2023.104948.

[7] C. Yan and N. Razmjooy, “Optimal lung cancer detection based on CNN optimized and improved Snake optimization algorithm,” *Biomedical Signal Processing and Control*, vol. 86, 2023, doi: 10.1016/j.bspc.2023.105319.

[8] V. Deepa and P. M. Fathimal, “Deep-shrimp Net fostered lung cancer classification from CT images,” *International Journal of Image, Graphics and Signal Processing*, vol. 15, no. 4, pp. 59–68, 2023, doi: 10.5815/ijigsp.2023.04.05.

[9] A. Saihood, H. Karshenas, and A. R. N. -Nilchi, “Multi-orientation local texture features for guided attention-based fusion in lung nodule classification,” *IEEE Access*, vol. 11, pp. 17555–17568, 2023, doi: 10.1109/ACCESS.2023.3243104.

[10] A. Bhattacharjee, R. Murugan, T. Goel, and S. Mirjalili, "Pulmonary nodule segmentation framework based on fine-tuned and pretrained deep neural network using CT images," *IEEE Transactions on Radiation and Plasma Medical Sciences*, vol. 7, no. 4, pp. 394–409, 2023, doi: 10.1109/TRPMS.2023.3236719.
[11] H. A. Helaly, M. Badawy, E. M. E.-Gendy, and A. Y. Haikal, "ELCD-NSC2: a novel early lung cancer detection and non-small cell classification framework," *Neural Computing and Applications*, vol. 36, no. 24, pp. 15149–15164, 2024, doi: 10.1007/s00521-024-09856-y.
[12] B. Spoorthi and S. Mahesh, "Hybrid optimized MRF based lung lobe segmentation and lung cancer classification using Shufflenet," *Multimedia Tools and Applications*, vol. 83, no. 17, pp. 52335–52364, 2023, doi: 10.1007/s11042-023-17570-5.
[13] C. S. Parvathy and J. P. Jayan, "Lung cancer prediction in chest CT using an active contour based segmentation and 3DCNN," *Multimedia Tools and Applications*, vol. 83, no. 21, pp. 60493–60517, 2023, doi: 10.1007/s11042-023-17792-7.
[14] A. Gupta, A. Kumar, and K. Rautela, "UDCT: lung cancer detection and classification using U-net and DARTS for medical CT images," *Multimedia Tools and Applications*, vol. 84, no. 18, pp. 19065–19085, 2024, doi: 10.1007/s11042-024-19801-9.
[15] L. Ma, C. Wan, K. Hao, A. Cai, and L. Liu, "A novel fusion algorithm for benign-malignant lung nodule classification on CT images," *BMC Pulmonary Medicine*, vol. 23, no. 1, 2023, doi: 10.1186/s12890-023-02708-w.
[16] J. M. Challab and F. Mardukhi, "Ant colony optimization–rain optimization algorithm based on hybrid deep learning for diagnosis of lung involvement in coronavirus patients," *Iranian Journal of Science and Technology, Transactions of Electrical Engineering*, vol. 47, no. 3, pp. 887–902, 2023, doi: 10.1007/s40998-023-00611-y.
[17] C. S. Parvathy and J. P. Jayan, "Automatic lung cancer detection using computed tomography based on chan vese segmentation and SENET," *Optical Memory and Neural Networks*, vol. 33, no. 3, pp. 339–354, 2024, doi: 10.3103/S1060992X2470022X.
[18] W. Li, G.-H. Liu, H. Fan, Z. Li, and D. Zhang, "Self-supervised multi-scale cropping and simple masked attentive predicting for lung CT-scan anomaly detection," *IEEE Transactions on Medical Imaging*, vol. 43, no. 1, pp. 594–607, 2024, doi: 10.1109/TMI.2023.3313778.
[19] A. B. Tofighi, A. Ahmadi, and H. Mosadegh, "Improving lung cancer detection via MobileNetV2 and stacked-GRU with explainable AI," *International Journal of Information Technology*, vol. 17, no. 2, pp. 1189–1196, 2025, doi: 10.1007/s41870-024-02045-z.
[20] L. Ma, H. Wu, and P. Samundeeswari, "GoogLeNet-AL: a fully automated adaptive model for lung cancer detection," *Pattern Recognition*, vol. 155, 2024, doi: 10.1016/j.patcog.2024.110657.
[21] Y. Kumaran S, J. J. Jeya, T. R. Mahesh, S. B. Khan, S. Alzahrani, and M. Alojail, "Explainable lung cancer classification with ensemble transfer learning of VGG16, Resnet50 and InceptionV3 using grad-cam," *BMC Medical Imaging*, vol. 24, no. 1, 2024, doi: 10.1186/s12880-024-01345-x.
[22] M. H. Sabzalian, F. Kharajinezhadian, A. Tajally, R. Reihanisaransari, H. A. Alkhazaleh, and D. Bokov, "New bidirectional recurrent neural network optimized by improved Ebola search optimization algorithm for lung cancer diagnosis," *Biomedical Signal Processing and Control*, vol. 84, 2023, doi: 10.1016/j.bspc.2023.104965.
[23] R. Raza *et al.*, "Lung-EffNet: lung cancer classification using EfficientNet from CT-scan images," *Engineering Applications of Artificial Intelligence*, vol. 126, 2023, doi: 10.1016/j.engappai.2023.106902.
[24] H. F. A.-Yasriy, "The IQ-OTH/NCCD lung cancer dataset," *Kaggle*. 2020. [Online]. Available: https://www.kaggle.com/datasets/hamdallak/the-iqothnccd-lung-cancer-dataset
[25] M. Kanipriya, C. Hemalatha, N. Sridevi, S. R. SriVidhya, and S. L. J. Shabu, "An improved capuchin search algorithm optimized hybrid CNN-LSTM architecture for malignant lung nodule detection," *Biomedical Signal Processing and Control*, vol. 78, 2022, doi: 10.1016/j.bspc.2022.103973.

BIOGRAPHIES OF AUTHORS

Kaliba Gowthami received bachelor's degree in Information Technology, M.Tech. in Computer Science Engineering, Chittoor, India. She has 9 years of teaching experience and now is currently TRA in VIT, Vellore. Her research interests include in medical imaging, machine learning, deep learning, and image processing. She can be contacted at email: gowthami.k2022@vitstudent.ac.in.

Kamalakannan Jayaseelan received bachelor's degree in Electronics and Communication Engineering, M.E. degree in Computer Science and Ph.D. degree in Computer Science from VIT university, Vellore, India. He has nearly 30 years of teaching experience. He is currently an associate professor senior with the School of Computer Science Engineering and Information Systems, VIT. He has published more than 30 articles in reputed journals in national and international level. His research interests include medical imaging, machine learning, deep learning, data analytics, and image processing. He can be contacted at email: jkamalakannan@vit.ac.in.